

On modeling of discrete propagation of localized damage in cohesive-frictional materials

E. Haghighat and S. Pietruszczak^{*,†}

Department of Civil Engineering, McMaster University, Hamilton, Ontario, Canada

SUMMARY

In this paper, the problem of propagation of localized deformation associated with formation of macrocracks/shear bands is studied in both tensile and compressive regimes. The main focus here is on enhancement of the constitutive law with embedded discontinuity to provide a discrete representation of the localization phenomenon. This has been accomplished by revising the formulation and coupling it with the level-set method for tracing the propagation path. Extensive numerical studies are conducted involving various fracture modes, ranging from brittle to frictional, and the results are compared with the experimental data as well as those obtained using XFEM methodology. Copyright © 2015 John Wiley & Sons, Ltd.

Received 21 August 2014; Revised 14 January 2015; Accepted 28 January 2015

KEY WORDS: embedded discontinuity model; XFEM; constitutive modeling; level-set method; localized deformation

1. INTRODUCTION

The research reported here is focused primarily on the problem of damage propagation in frictional materials. The approach incorporates a constitutive law with embedded discontinuity (CLED). This methodology, developed in references [1, 2], has been previously used within the context of *smeared* modeling of localization problems. The primary novelty here is an extension of this framework to describe the *discrete* nature of the frictional damage process associated with elastoplastic deformation. This has been achieved by revising the original approach and coupling it with the level-set representation to capture the path of the macrocrack/shear band propagation. Within the proposed framework, the discontinuity is defined at the element level rather than at an integration point, which is in contrast to the classical smeared approach. Thus, in the presence of a discontinuous motion, the volume of a finite element itself is perceived as a reference volume. In what follows, an analytical derivation of the governing equations is provided first based on averaging the motion characteristics in the vicinity of discontinuity. An implicit return mapping algorithm is then developed for integration of the governing elastoplastic constitutive relation. A simple numerical strategy is also introduced for specifying the direction of propagating macrocrack based on orientation averaging in the domain adjacent to the tip. The framework is subsequently applied to numerical analysis of problems involving a cohesive/mixed-mode fracture as well as strain localization associated with formation of a shear band, and the results are compared with those obtained from Extended Finite Element Method (XFEM) simulations.

Since the rise of the computational era in the 1960s, an intensive amount of research has been conducted on modeling of the evolution of damage. The focus was initially on brittle materials, and

^{*}Correspondence to: S. Pietruszczak, Department of Civil Engineering, McMaster University, Hamilton, Ontario, L8S 4L7, Canada.

[†]E-mail: pietrusz@mcmaster.ca

one of the first attempts, within the finite element framework, was based on separating the element edges during the crack formation process [3, 4]. In order to improve the accuracy, this approach was later combined with adaptive re-meshing [5–7]; however, it proved to be computationally inefficient. The other methodology that was pursued was the smeared cracking approach. This approach was initiated in the late 1960s in a work by Rashid [8]. Because of its simplicity and suitability in FEM formulation, it has been widely used in the 1970s and 1980s for modeling of damage [9–12]. The approach is well suited for simulating the evolution of cracking in brittle materials, like concrete, at early stages of the loading process, as the damage is then associated with formation of multiple microcracks within the considered domain. However, the macrocracking and its discrete nature cannot be properly modeled within this approach. Furthermore, the formulation suffers from mesh size dependence. An alternative approach to address the issues related to discrete crack propagation involves the boundary integral formulation [13]. The framework is consistent with that of the linear fracture mechanics; it can provide very accurate results in relation to the analytical solutions; however, its extension to deal with material nonlinearity is complex. The next approach that was developed was the one presented in reference [1]. The methodology was based on a smeared representation, incorporating volume averaging, and the focus was on resolving the issue related to the mesh size dependence. This was accomplished by incorporating a characteristic dimension that was explicitly related to geometry of the discretized domain. An attempt conceptually similar to this work was later presented in reference [14] following a different mathematical format.

Another way to incorporate the strong discontinuities within the FEM approximation space was the use of elements with embedded discontinuities [15] and/or regularized discontinuous finite elements [16]. In addition, element-free Galerkin methods have also been employed for simulating the damage evolution as they show higher accuracy compared with standard FEM interpolations [17]. Introduction of reproducing kernel and partition-of-unity concepts [18–20] has opened a new door in numerical modeling of crack propagation and led to the introduction of the XFEM [21–23]. This approach is well suited for describing the discrete nature of the crack propagation process, and an extensive research has been conducted on this topic over the last few decades. The approach has been coupled with the level-set method for tracing the propagating crack [24, 25] and later used in modeling the discontinuities in a wide range of applications including dynamic problems [26], hydro-mechanical problems [27–29], thermo-elasticity [30–32], contact problems [33, 34], and shear band formation [35, 36]. The approach has also been used for discontinuous modeling within the newly developed isogeometric method [37].

In this article, the problem of damage propagation associated with shear band localization is investigated. As mentioned earlier, the main focus here is on employing FEM that incorporates an enhanced CLED approach. The enhancement deals with proposing a strategy to capture the path of damage propagation in a discrete way and coupling of this methodology with the level-set representation. The results are compared with experimental evidence and/or those obtained using the XFEM approach. In Section 2.1, the analytical representation of a discontinuous motion along with its implementation in the XFEM is reviewed. Section 2.2 focuses on the formulation of a constitutive law incorporating a strong discontinuity, which is then followed, in Section 3, by the formulation of a new return mapping scheme. The enhanced crack propagation strategy that is used within this framework is outlined in Section 4. In Section 5, the results of extensive numerical studies are discussed. First, some illustrative examples dealing with cohesive crack propagation are provided, which include a double-cantilever problem investigated in [38] and the simulation of a mixed-mode cracking test performed in [39]. Later, the problems involving shear band localization are examined, including the simulation of a plane strain biaxial compression test [40] as well as an assessment of slope stability. It is demonstrated that both frameworks, that is, FEM incorporating the enhanced CLED and XFEM, yield virtually identical response, thus giving advantage to the former one as it does not require the incorporation of any additional DOFs. The conclusions emerging from this study are presented in Section 6. All simulations conducted here are based on FEM/CLED and XFEM programs that were developed by the authors.

2. DISCONTINUOUS MOTION: XFEM VERSUS CONSTITUTIVE LAW WITH EMBEDDED DISCONTINUITY

Referring to Figure 1, consider a body Ω that includes a discontinuous surface Γ_d . The discontinuity can be described as $\Gamma_d = \{x_\alpha | x_\alpha \in \Omega \wedge \phi(x_\alpha) = 0\}$, where $\phi(x_\alpha)$ is the signed distance function that can be expressed as $\phi(x_\alpha) = \text{sign}(n_\alpha(x_\alpha - \tilde{x}_\alpha)) \min \|x_\alpha - \tilde{x}_\alpha\|$, while $\tilde{x}_\alpha = \{x_\alpha | x_\alpha \in \Gamma_\alpha\}$ and α is the coordinate indicator. The normal vector \tilde{n}_i to the interface Γ_d can be defined as $\tilde{n}_i = \phi_{,i} / \|\phi_{,i}\|$. The latter is directed from Ω^- to Ω^+ , and thus, the tangential vector \tilde{m}_i may be expressed as a result of a counterclockwise 90° rotation of \tilde{n}_i , as shown in Figure 1.

Within this body, a discontinuous motion $v_i(x_\alpha, t)$ can be described as a sum of two continuous functions $\hat{v}_i(x_\alpha, t)$ and $\tilde{v}_i(x_\alpha, t)$ combined with a discontinuous step function \mathcal{H}_{Γ_d} , that is,

$$v_i(x_\alpha, t) = \hat{v}_i(x_\alpha, t) + \mathcal{H}_{\Gamma_d} \tilde{v}_i(x_\alpha, t) \quad (1)$$

Here, $\mathcal{H}_{\Gamma_d} = \mathcal{H}(\phi)$ is the Heaviside function that can be expressed in its symmetric form as

$$\mathcal{H}(\phi) = 2 \int_{-\infty}^{\phi} \delta(\varphi) d\varphi - 1 = \begin{cases} +1 & \phi \geq 0 \\ -1 & \phi < 0 \end{cases} \quad (2)$$

where $\delta(\phi)$ is the Dirac delta function that is defined as singular at $\phi = 0$ and zero elsewhere. Denoting a jump of a function at the point $x_\alpha = \tilde{x}_\alpha$ located on discontinuity surface Γ_d as $[\![\bullet]\!] = \bullet^+ - \bullet^-$, the discontinuous motion \dot{g}_i can be defined as

$$\dot{g}_i = [\![v_i]\!] = \hbar \tilde{v}_i \quad (3)$$

where \hbar is the jump of the Heaviside function at $x_\alpha = \tilde{x}_\alpha$ and can be evaluated as $\hbar = \mathcal{H} = \mathcal{H}^+ - \mathcal{H}^-$. Based on the representation (2), it can be shown that $\hbar = 2$. Considering that $\mathcal{H}_{,i}(\phi) = \mathcal{H}' \phi_{,i}$ and $\mathcal{H}'(\phi(x_\alpha)) = \hbar \delta(\phi(x_\alpha)) = \hbar \delta_{\Gamma_d}$, the velocity gradient of the discontinuous motion (1) can be expressed as

$$v_{i,j}(x_\alpha, t) = \hat{v}_{i,j}(x_\alpha, t) + \mathcal{H}_{\Gamma_d} \tilde{v}_{i,j}(x_\alpha, t) + \delta_{\Gamma_d} \dot{g}_i(t) \tilde{n}_j \quad (4)$$

where $\tilde{n}_i = \phi_{,i}$ is the normal to the interface, as defined earlier.

2.1. Incorporation of discontinuous motion into the finite element approach: XFEM

Based on the partition-of-unity property of FEM interpolations, the enriched shape functions can be directly incorporated into the approximation space through the generalized FEM or XFEM. Thus, the discontinuous motion (1) can be approximated by

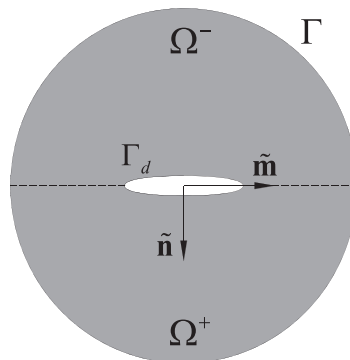


Figure 1. A body Ω with a discontinuity Γ_d .

$$v_i^h(x_a, t) = \hat{v}_i^h(x_a, t) + \mathcal{H}_{\Gamma_d} \tilde{v}_i^h(x_a, t) = \sum_{I \in \hat{I}} \hat{N}_I(x_a) \dot{\hat{d}}_{Ii}(t) + \sum_{I \in \tilde{I}} \mathcal{H}(\phi(x_a)) \tilde{N}_I(x_a) \dot{\tilde{d}}_{Ii}(t) \quad (5)$$

where \hat{N}_I and \tilde{N}_I are standard finite element shape functions, \hat{I} and \tilde{I} are sets of standard and enriched nodes, and $\dot{\hat{d}}_{Ii}(t)$ and $\dot{\tilde{d}}_{Ii}(t)$ are standard and enriched DOFs associated with node I and direction i , respectively. In order to achieve a better representation of the enriched approximation and to avoid the use of blending elements, the shifted form of the enrichment function \mathcal{H} can be used, that is, $\psi^I(x_a) = \mathcal{H}(\phi(x_a)) - \mathcal{H}(\phi(x_a^I))$, as introduced in [41]. Note that the crack opening $\dot{g}_i^h(x_a, t) = \llbracket v_i^h(x_a, t) \rrbracket$ can be expressed as

$$\dot{g}_i^h(x_a, t) = \sum_{I \in \hat{I}} \llbracket \hat{N}_I(x_a) \rrbracket \dot{\hat{d}}_{Ii}(t) + \sum_{I \in \tilde{I}} \llbracket \psi^I(x_a) \tilde{N}_I(x_a) \rrbracket \dot{\tilde{d}}_{Ii}(t) = \hbar \sum_{I \in \tilde{I}} \tilde{N}_I(x_a) \dot{\tilde{d}}_{Ii}(t) \quad (6)$$

where \hbar is the jump in the shifted enrichment function, that is, $\hbar = \mathcal{H}^+ - \mathcal{H}^-$.

2.2. Constitutive law with embedded discontinuity (CLED)

In order to incorporate a discontinuous motion into a constitutive model, one can invoke the additivity postulate, similar to that employed in plasticity. Thus, the total strain rate $\dot{\varepsilon}_{ij}$ can be decomposed into $\tilde{\varepsilon}_{ij}$, which describes the deformation in the intact part of the reference volume, and $\dot{\tilde{\varepsilon}}_{ij}$, which is due to the discontinuous motion along the interface, that is,

$$\dot{\varepsilon}_{ij} = \tilde{\varepsilon}_{ij} + \dot{\tilde{\varepsilon}}_{ij} \quad (7)$$

The strain rate $\dot{\tilde{\varepsilon}}_{ij}$ itself can be decomposed into an elastic part and a plastic part, namely $\dot{\tilde{\varepsilon}}_{ij} = \dot{\tilde{\varepsilon}}_{ij}^e + \dot{\tilde{\varepsilon}}_{ij}^p$. In order to define a proper measure for the discontinuous strain rate, Eq. (4) can be employed, which provides an analytical representation of a motion that includes a discontinuity. As can be seen from this equation, there are two parts associated with the motion; one is defined as $v_{i,j} = \hat{v}_{i,j} + \mathcal{H} \tilde{v}_{i,j}$ and describes the motion in the intact material, while the other one is associated with the discontinuous motion along the interface, that is, $\delta_{\Gamma_d}(\dot{g}_i n_j)$. It is clear that the first part leads to the strain rate in the intact part of the body, whereas the discontinuous part describes the strain rate due to the deformation within the interfacial material. It is evident from the nature of the Dirac delta function that this component acts only along the interface and it can be distributed over a small enough reference volume through an averaging procedure. Thus, taking the volume average of this term, the discontinuous strain $\dot{\tilde{\varepsilon}}_{ij}$ can be defined as

$$\dot{\tilde{\varepsilon}}_{ij} = \frac{1}{\Delta v} \int_{\Delta v} \delta_{\Gamma_d}(\dot{g}_i n_j)^s dv = \frac{1}{\Delta v} \int_{\Delta a} (\dot{g}_i n_j)^s da \quad (8)$$

where the superscript s refers to the symmetric part of the operator and Δa is the area of the discontinuity inside the given reference volume Δv . Considering the last integral to represent an average value of the dyadic product $\dot{g}_i n_j$ over the differential area Δa and defining $\chi = \Delta a / \Delta v$, one can approximate Eq. (8) as

$$\dot{\tilde{\varepsilon}}_{ij} = \frac{\Delta a}{\Delta v} (\dot{g}_i n_j)^s \quad (9)$$

In conclusion, the strain decomposition including discontinuous motion can now be expressed as

$$\dot{\varepsilon}_{ij} = \dot{\tilde{\varepsilon}}_{ij} + \dot{\tilde{\varepsilon}}_{ij}^p = \dot{\tilde{\varepsilon}}_{ij}^e + \dot{\tilde{\varepsilon}}_{ij}^p + \chi(\dot{g}_i n_j)^s \quad (10)$$

Note that the representation (10) is, in fact, identical to the strain decomposition introduced in reference [2]. In Eq. (10), one can interpret $\dot{\tilde{\varepsilon}}_{ij}$ as the deformation in the intact material and $\dot{\tilde{\varepsilon}}_{ij}^p$ as the discontinuous motion averaged over the corresponding reference volume. It should be noted that in contrast to XFEM, where additional DOFs are introduced as external variables, the current representation employs unknown rates of velocity discontinuities \dot{g}_i , which can be defined through a plasticity-based approach by imposing the continuity condition along the interface.

The strain localization is typically associated with an elastic response of the intact material. Thus, in order to formulate the problem, we can invoke the elastic constitutive operator, so that

$$\dot{\sigma}_{ij} = D_{ijkl}^e (\dot{\varepsilon}_{kl} - \dot{\tilde{\varepsilon}}_{kl}) = D_{ijkl}^e \dot{\varepsilon}_{kl} - D_{ijkl}^e (\chi \dot{g}_k n_l) \quad (11)$$

Now, the interfacial constitutive model relates the rate of traction, which is a function of the discontinuous motion, to the velocity discontinuity \dot{g}_i . Thus, $\dot{t}_i = K_{ij} \dot{g}_j$, where K_{ij} is the tangential stiffness operator for the interface material. By imposing the continuity condition $n_i \dot{\sigma}_{ij} = \dot{t}_j = K_{ji} \dot{g}_i$ along the interface, the velocity discontinuity can be expressed as

$$\dot{g}_i = \left(K_{ip} + \chi n_r D_{rjps}^e \right)^{-1} n_q D_{pqkl}^e \dot{\varepsilon}_{kl} \quad (12)$$

Using now the relation (9), the associated discontinuous strain rate can be defined as

$$\dot{\tilde{\varepsilon}}_{ij} = E_{ijpq} D_{pqkl}^e \dot{\varepsilon}_{kl}; \quad E_{ijpq} = \chi n_i \left(K_{jp} + \chi n_r D_{rjps}^e n_s \right)^{-1} n_q \quad (13)$$

Therefore, the constitutive relation for the case of embedded discontinuity takes the form

$$\dot{\sigma}_{ij} = \tilde{D}_{ijkl} \dot{\varepsilon}_{kl}; \quad \tilde{D}_{ijkl} = D_{ijkl}^e - D_{ijpq}^e E_{pqrs} D_{rskl}^e \quad (14)$$

It should be pointed out that, unlike in the original smeared representation, the discontinuity is defined here at the element level, not at individual Gauss points, and it is traced by the level-set method; thus, the location and orientation of the crack are known exactly, as in XFEM. In this way, the value of the characteristic dimension $\chi = \Delta a / \Delta v$ can be accurately assessed.

It is noted that if the intact material undergoes plastic deformation, the stress rate $\dot{\sigma}_{ij}$ should be defined as

$$\dot{\sigma}_{ij} = \tilde{D}_{ijkl} (\dot{\varepsilon}_{kl} - \dot{\tilde{\varepsilon}}_{kl}^p) \quad (15)$$

In this case, the yield function f and the non-associated flow rule can be expressed as

$$f = f(\sigma_{ij}, \kappa) \leq 0; \quad \psi = \psi(\sigma_{ij}) = \text{const}; \quad \dot{\tilde{\varepsilon}}_{ij}^p = \dot{\lambda} \frac{\partial \psi}{\partial \sigma_{ij}} \quad (16)$$

where κ is a hardening parameter. For an active loading process, the consistency condition can be written as

$$\dot{f} = \frac{\partial f}{\partial \sigma_{ij}} \dot{\sigma}_{ij} + \frac{\partial f}{\partial \kappa} \frac{\partial \kappa}{\partial \lambda} \dot{\lambda} = 0 \quad (17)$$

Substituting now the stress rate defined in Eq. (15) one obtains, after some algebraic manipulations

$$\dot{\lambda} = \frac{1}{H} \frac{\partial f}{\partial \sigma_{ij}} \tilde{D}_{ijkl} \dot{\epsilon}_{kl}; \quad H = \frac{\partial f}{\partial \sigma_{ij}} \tilde{D}_{ijkl} \frac{\partial \psi}{\partial \sigma_{kl}} - \frac{\partial f}{\partial \kappa} \frac{\partial \kappa}{\partial \lambda} \quad (18)$$

Thus, by substituting relations (18) back into (15), the tangential stiffness operator can be defined as

$$\dot{\sigma}_{ij} = D_{ijkl} \dot{\epsilon}_{kl}; \quad D_{ijkl} = \tilde{D}_{ijkl} - \frac{1}{H} \tilde{D}_{ijkl} \frac{\partial \psi}{\partial \sigma_{kl}} \frac{\partial f}{\partial \sigma_{rs}} \tilde{D}_{rskl} \quad (19)$$

In conclusion, for the elements that experience the localized deformation in the form of a macrocrack/shear band, the trial stress rate can be found using Eq. (14), that is, assuming a linear response of the intact material. If the trial stress does not violate the loading condition, no correction is required. If not, that is, in the case of an active plastic process, the stress increment and the tangential operator must be updated based on relation (19).

3. IMPLICIT INTEGRATION SCHEME FOR CONSTITUTIVE LAW WITH EMBEDDED DISCONTINUITY

For the completeness of the presentation, the numerical integration scheme is briefly discussed here. In the case of XFEM analysis, the nonlinearity of the interfacial material is handled within the Newton–Raphson solver itself, as the discontinuous motion \dot{g}_i is an external variable. At the same time, the nonlinearity of the intact material can be dealt with using a standard implicit integration scheme. The implementation of CLED requires, however, a development of an appropriate return mapping algorithm, which is presented in the following.

The procedure invokes the specification of trial stress that is assessed using the elastic stiffness operator. Thus, for an element with embedded discontinuity, the trial stress can be expressed as

$$\sigma_{ij}^{trial} = \sigma_{ij}^t + \tilde{D}_{ijkl} \Delta \epsilon_{kl} \quad (20)$$

where \tilde{D}_{ijkl} is defined in Eq. (14). Once the trial stress is determined, the value of the yield function must be evaluated. In the case where $f^{trial}(\sigma_{ij}^{trial}, \kappa^t) < 0$ or $f^{trial}(\sigma_{ij}^{trial}, \kappa^t) = 0 \wedge (\partial f / \partial \sigma_{ij}) \Delta \sigma_{ij} < 0$, the material remains in the elastic range, so that the representation (14) results in a correct response. For the case of an active loading process, that is, $f^{trial} = f(\sigma_{ij}^{trial}, \kappa^t) > 0$, according to the return mapping scheme [42], the residuals at iteration v can be written in terms of stress and plastic strain increment at $t + \Delta t$ as

$$\begin{aligned} r_{ij}^v &= \sigma_{ij}^v - \left(\sigma_{ij}^t + \tilde{D}_{ijkl} (\Delta \epsilon_{kl} - \Delta \epsilon_{kl}^{p,v}) \right) \\ f^v &= f(\sigma_{ij}^v, \kappa^v) \end{aligned} \quad (21)$$

Using Newton–Raphson algorithm, residual (21) can be expressed as

$$\begin{aligned}
 r_{ij}^{v+1} &\approx r_{ij}^v + \frac{\partial r_{ij}}{\partial \sigma_{mn}} \delta \sigma_{mn}^v + \frac{\partial r_{ij}}{\partial \lambda} \delta \lambda^v = 0 \\
 f^{v+1} &\approx f^v + \frac{\partial f^v}{\partial \sigma_{mn}} \delta \sigma_{mn}^v + \frac{\partial f^v}{\partial \lambda} \delta \lambda^v = 0
 \end{aligned}
 \quad (22)$$

Solving now Eq. (22) for $(\delta \lambda, \delta \sigma_{ij})^v$ yields

$$\delta \lambda^v = \frac{f^v - \frac{\partial f}{\partial \sigma_{ij}} Q_{ijkl}^{-1} r_{kl}^v}{\frac{\partial f}{\partial \sigma_{ij}} Q_{ijkl}^{-1} \tilde{D}_{klmn} \frac{\partial \psi}{\partial \sigma_{mn}} - \frac{\partial f}{\partial \kappa} \frac{\partial \kappa}{\partial \lambda}}, \quad \delta \sigma_{ij}^v = -D_{ijkl} \frac{\partial \psi}{\partial \sigma_{kl}} \delta \lambda^v \quad (23)$$

where $Q_{ijkl} = \delta_{ij} \delta_{kl} + \Delta \lambda (\partial^2 \psi / \partial \sigma_{ij} \partial \sigma_{kl})$. Note that if increments are small enough, $\Delta \lambda \rightarrow 0$, one obtains $Q_{ijkl} \approx \delta_{ij} \delta_{kl}$. Thus, stress updates can be expressed as

$$\begin{aligned}
 \Delta \sigma_{ij}^{v+1} &= \Delta \sigma_{ij}^v + \delta \sigma_{ij}^v \\
 \Delta \lambda^{v+1} &= \Delta \lambda^v + \delta \lambda^v
 \end{aligned}
 \quad (24)$$

This correction process must be continued until convergence is achieved, that is, $f(\sigma_{ij}^{v+1}, \kappa^{v+1}) \leq 0$. Note that at the end of each iteration, Δg_i , $\Delta \sigma_{ij}$, and D_{ijkl} must be updated as the discontinuous motion $\Delta \dot{g}_i$ is a function of the stress state.

4. CRACK PROPAGATION STRATEGY: INITIATION AND TRACING THE DIRECTION

The assessment of the onset of localized deformation, which is associated with formation of macrocracks and/or shear bands, involves different approaches that include bifurcation analysis [43], critical plane framework [44], and non-local criteria for pre-existing defects [45]. A simplified approach that is most frequently employed incorporates an assumption that the localization occurs when the trajectory describing the given stress state approaches the failure surface, which is defined as a local path-independent criterion. For simplicity, the latter approach is followed here, whereby the maximum tensile strength criterion (for the cohesive crack propagation) and the Mohr–Coulomb criterion (for the description of frictional shear band formation) are employed.

As proposed in a number of previous studies, for example, [24], the level-set method can be used for tracing the propagating crack. Based on this methodology, a moving/propagating interface $\Gamma_d(t)$ can be defined as the zero level set of a function $\phi(x_\alpha, t)$, that is, $\Gamma_d(t) = \{x_\alpha | \phi(x_\alpha, t) = 0\}$. A function that can represent such a property is the signed distance function as proposed in [46]. For the numerical simulations conducted here, the level-set method has been coupled with both XFEM and FEM/CLED.

In most of the published works, the J-integral method is used to evaluate the stress intensity factors and to define the direction of the crack propagation. However, the main drawback associated with this method is that it is limited to elastic–brittle materials that undergo a tensile damage. As mentioned earlier, a simple and effective way of defining the onset of fracture and the direction of the propagating crack is to invoke a specific form of the failure criterion. For failure in tension, for example, the maximum tensile stress criterion may be employed, which stipulates that the direction of the crack is perpendicular to that of the major principal stress. In the case of frictional materials, commonly described by the Mohr–Coulomb criterion, the crack is also said to form at a prescribed orientation, that is, $\pm(45 + \phi/2)$ relative to the direction of the minor principal stress. It should be pointed out that the integral approaches, such as the J-integral method, have an implicit averaging nature, that is, they provide average measures defined over a domain of interest. Using a similar concept of average property, a simple algorithm is implemented here for assessing the direction of propagation of the discontinuity surface. In a typical scenario, the stress state at most integration

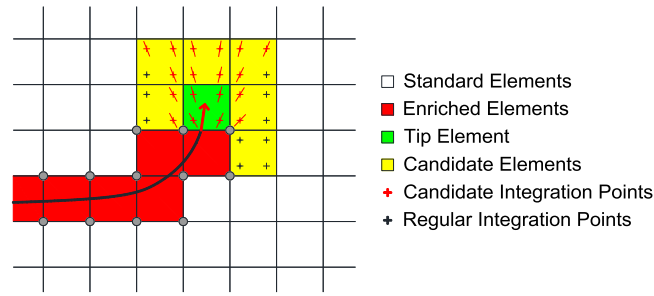


Figure 2. Crack propagation methodology used for both XFEM and FEM/CLED.

points in the vicinity of the crack tip is close to the failure envelope. Therefore, the scheme used here for assessing the direction of propagation is based on checking the failure criterion at the integration points adjacent to the tip element. The average direction of propagation is then established based on the orientations associated with the neighboring integration points. This algorithm is illustrated schematically in Figure 2. Note that by implementing this methodology, a stable crack pattern propagation is achieved for both XFEM and CLED, which is not the case without incorporation of the averaging scheme.

5. NUMERICAL SIMULATIONS

In this section, different boundary value problems are examined involving both FEM with a discontinuity embedded within the constitutive relation and XFEM. Note that XFEM is used here as a verification tool for assessing the accuracy of the results based on FEM/CLED formulation. The primary focus is on examining the damage propagation in frictional materials; however, for a more complete representation, some illustrative examples involving cohesive crack propagation are also provided. The key results are discussed in two separate sections; each section starting with a brief review of the interfacial model that is employed for the associated numerical study. For the case of crack propagation, the first example is based on the work reported in [38], while the second one incorporates the results of an experimental study conducted in [39]. For the strain localization involving a shear band formation, a plane strain biaxial test reported in reference [40] is simulated first. This study also involves an examination of the issue of sensitivity of the solution to mesh size/alignment. Later, numerical simulations involving an assessment of stability of a slope excavated in a material with an apparent cohesion are provided. All simulations reported here involve two-dimensional configurations.

5.1. Cohesive crack propagation: interface model and the results of numerical simulations

For this study, a cohesive crack model with an exponential decay has been employed (after reference [47]). Within this framework, the tensile strength of the material is defined as

$$\mathcal{F}_t(g_n) = F_t \exp\left(\frac{-F_t}{G} g_n\right) \quad (25)$$

where F_t is the initial strength at the onset of fracture, G is the fracture energy release rate, and $\mathcal{F}_t(g_n)$ is the tensile strength at separation g_n . The failure function is defined as

$$f(t_n, g_n) = t_n - \mathcal{F}_t(g_n) \quad (26)$$

For an active loading process, setting $f(t_n, g_n)=0$ will clearly result in $t_n = \mathcal{F}_t(g_n)$. For the simulations conducted here, it was assumed that tangential component of cohesive force is

negligible, that is, $t_m = 0$. Therefore, the constitutive relation in the local coordinate system, along the crack, can be expressed as

$$t_i^* = K_{ij}^* g_j^*; \quad K_{ij}^* = \begin{cases} -\frac{F_t^2}{G_f} \exp\left(-\frac{F_t}{G_f} g_n\right) & i = j = 1 \\ 0 & \text{otherwise} \end{cases} \quad (27)$$

where K_{ij}^* is the tangential operator.

5.1.1. Double-cantilever beam test. The first example involves the simulation of mode 1 crack propagation in a double-cantilever beam. The geometry and the boundary conditions are shown in Figure 3 and were chosen based on the information provided in reference [38]. The beam has dimensions of 400×200 mm with a thickness of 1000 mm; the notch is 120×12.5 mm. Because of the symmetry, only half of the domain was discretized. Following the original reference, a total number of 1005 structured quadrilateral elements were employed. The beam was analyzed under plane stress condition.

The load consisted of applying the vertical displacement at point A of the beam, and the material properties were taken as

$$E = 36.5 \text{ GPa}, \quad f_t = 3 \text{ MPa}, \quad \nu = 0.18, \quad G_f = 3 \text{ N/m} \quad (28)$$

Note that the value of G_f , assumed after reference [38], is quite low, which is indicative of a relatively high strain-softening rate. Reference [38] provides a detailed discussion on the influence of G_f on the solution, in particular on the issue of convergence.

The resultant force-versus-displacement characteristics are depicted in Figure 4 for FEM/CLED as well as XFEM simulations. It is noted that, for both solutions, the descending branch exhibits some oscillations, which are purely numerical. The problem may be rectified by incorporating more refined implicit/explicit integration schemes (cf. [38]). The cracking pattern superimposed on the vertical displacement field is shown in Figure 5. It is evident here that virtually identical response is obtained from both methodologies, in terms of the cracking pattern as well as the mechanical characteristics.

5.1.2. Mixed-mode cracking of concrete. The example given here involves the simulation of experimental tests conducted by Galvez and his co-workers [39] at Delft University. The geometry of the problem is shown in Figure 6. The problem involves a four-point bending of a notched concrete beam under the action of two independent actuators.

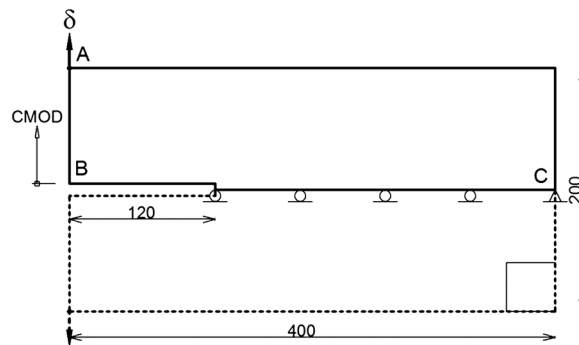


Figure 3. Geometry and boundary conditions for the double-cantilever beam (CMOD – crack mouth opening displacement).

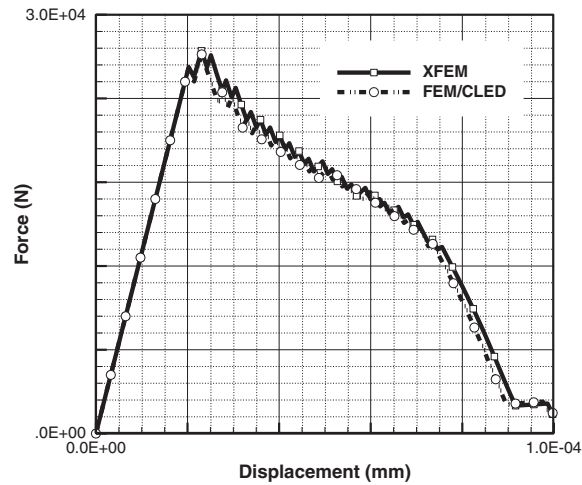


Figure 4. Force displacement response of the structure.

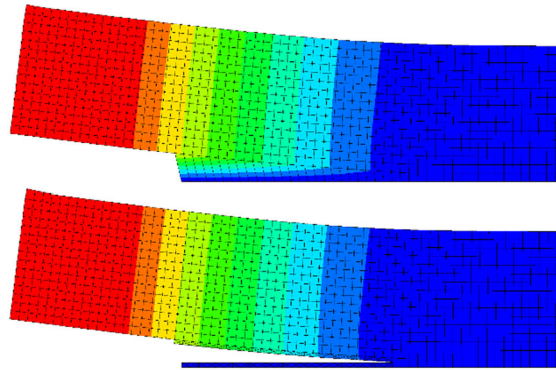


Figure 5. Cracking pattern from both FEM/CLED and XFEM simulations superimposed on vertical displacement contours.

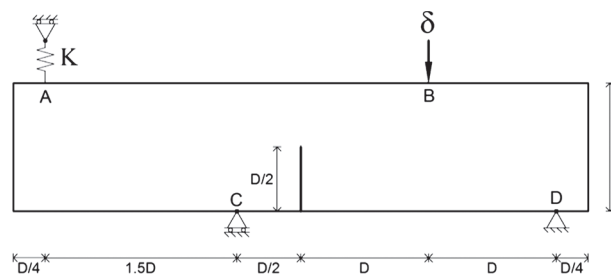


Figure 6. Mixed-mode cracking problem: geometry and boundary conditions.

In the original experimental studies, the specimens were tested at different values of D and K . The simulations conducted here correspond to $D = 300$ mm and involve two limiting cases of the value of K , namely, $K = 0$ (no constraint) and $K \rightarrow \infty$ (point A fixed). The problem was again considered as plane stress and was analyzed as displacement controlled (viz. δ). The material properties were taken as follows:

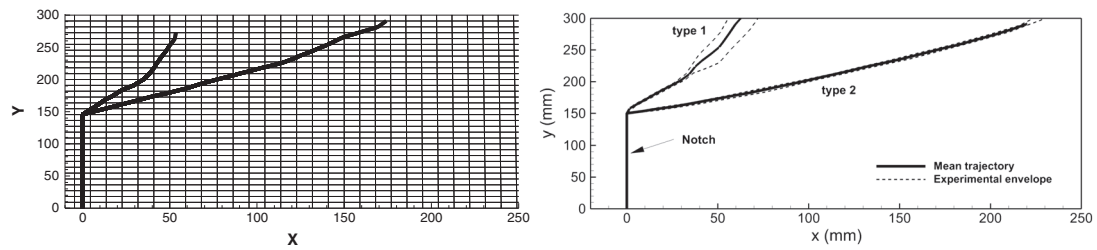


Figure 7. Left: cracking pattern from FEM/CLED and XFEM analysis. Right: experimental results [39].

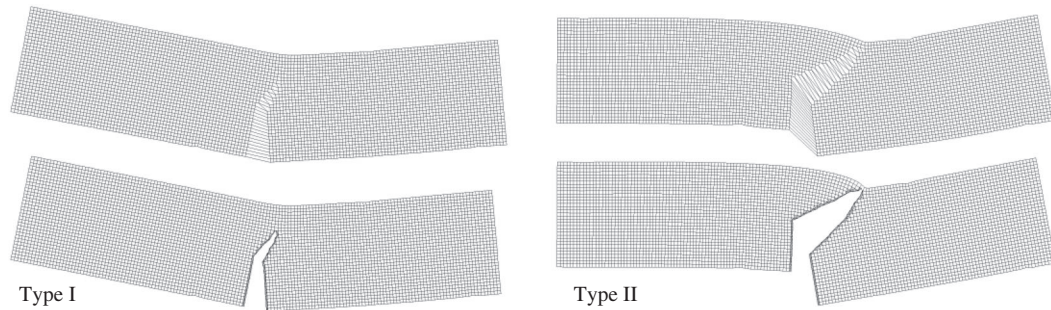


Figure 8. Deformed shape for both FEM/CLED and XFEM simulations; left: $K=0$ and right: $K \rightarrow \infty$.

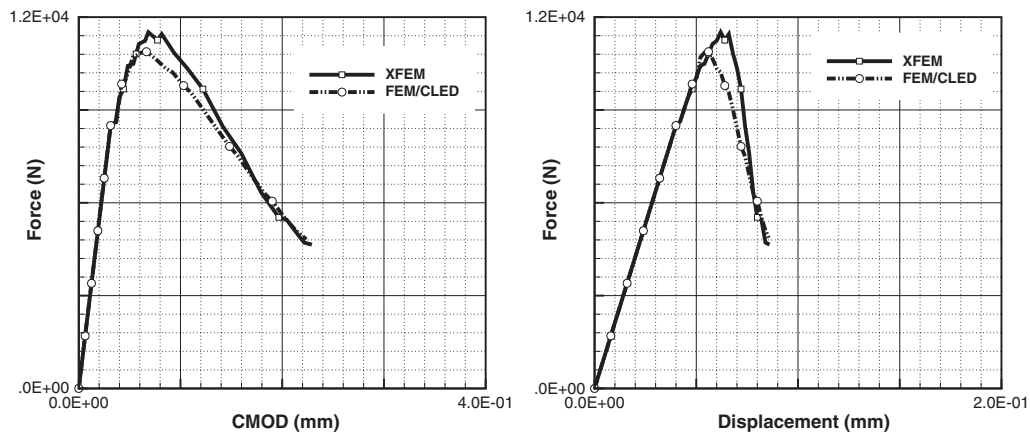


Figure 9. Load versus crack mouth opening displacement and load versus vertical displacement response ($K=0$).

$$E = 38 \text{ GPa}, \quad \nu = 0.2, \quad f_t = 3 \text{ MPa}, \quad G_f = 70 \text{ N/m} \quad (29)$$

while the thickness was assumed to be equal to 50 mm.

The cracking pattern, for both cases considered in the analysis, is shown in Figure 7 together with the relevant experimental data. Figure 8 shows the scaled images of the deformed shape for FEM/CLED as well as XFEM simulations. The load versus crack mouth opening displacement and load–vertical displacement characteristics are plotted in Figures 9 and 10, respectively. It is quite evident that the predictions using both methodologies are virtually identical and are fairly consistent with the experimental data reported in reference [34].

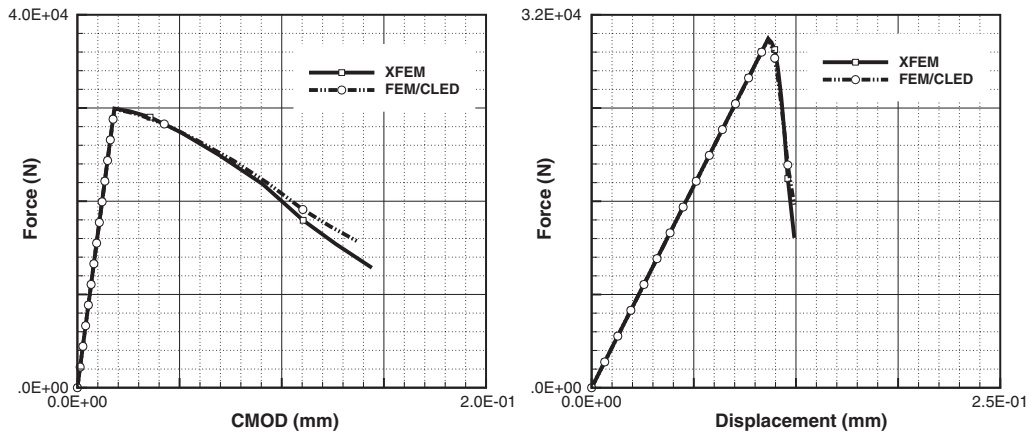


Figure 10. Load versus crack mouth opening displacement and load versus vertical displacement response ($K \rightarrow \infty$).

5.2. Shear band localization: interface model and the results of numerical simulations

For the case involving localized deformation associated with the inception of a shear band, a frictional contact model is incorporated. The yield and the plastic potential surfaces are defined as

$$f(t_n, t_m) = |t_m| + \mu(\gamma)(t_n + c) = 0; \quad \psi(t_m) = |t_m| = \text{const}; \quad \gamma = |g_m| \quad (30)$$

where (t_n, t_m) are the normal and tangential components of the traction vector, g_m is the tangential displacement along the interface, and γ is the strain-softening parameter that is identified with g_m . The softening function is assumed in an exponential form

$$\mu = \mu_r + (\mu_0 - \mu_r)\exp(\alpha\gamma) \quad (31)$$

where μ_0 is the value of friction coefficient at failure, μ_r is the residual value, and the parameter α controls the rate of softening. The constitutive relation can be formulated by invoking the standard plasticity formalism.

5.2.1. Modeling of localized deformation in a biaxial test on dense sand. The numerical analysis carried out here involves the simulation of a biaxial (plane strain) test conducted on a dense Ottawa sand at the confinement of 100 kPa [40]. The sample had dimensions of $83.3 \times 152.4 \times 80.8$ mm, and the deformation was recorded by digital monitoring of nodal displacements of the grid that was imprinted on the membrane surface (Figure 11).

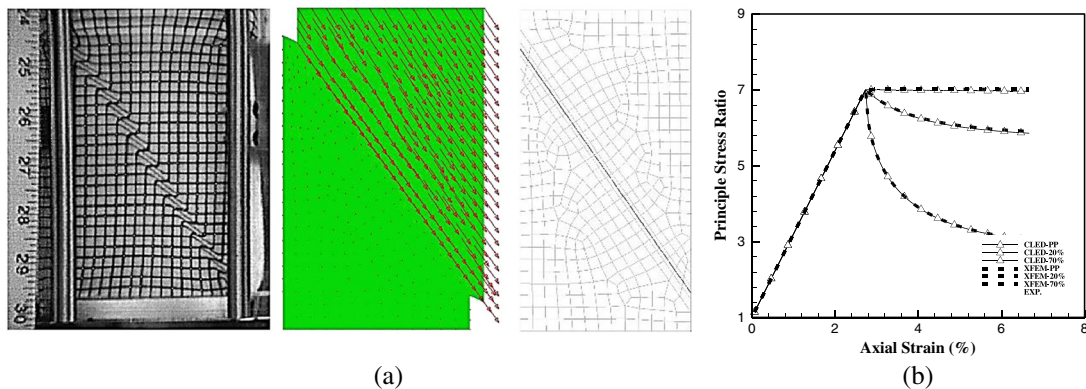


Figure 11. Shear band formation in biaxial plane strain test: (a) cracking pattern and post-localization deformation mode and (b) load-axial displacement curve.

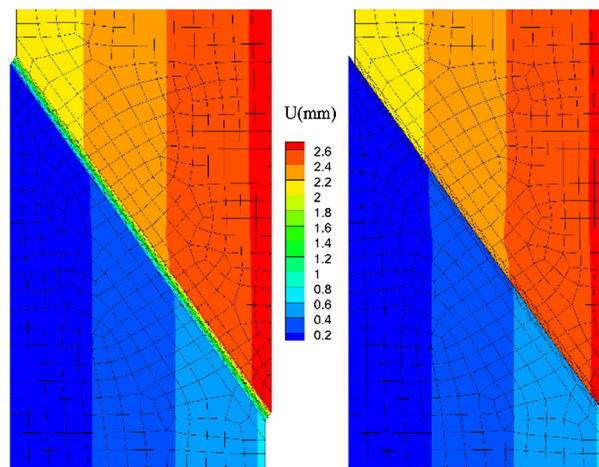


Figure 12. Post-failure response of the sample; left: FEM/CLED; right: XFEM analysis.

The simulations were carried out assuming that the material remains elastic prior to the onset of localization. The latter was defined as $\eta \rightarrow \eta_f$ in the classical Mohr–Coulomb criterion. In the softening regime, the response was said to be associated with a localized deformation mode, whereby the behavior of the shear band material was described through the interfacial constitutive model defined viz. Eq. (30). The key material properties, as reported in reference [40], were as follows:

$$E = 23 \text{ MPa}, \quad \nu = 0.3, \quad \phi = 48.2^\circ$$

where ϕ is the friction angle. For the interface, three different values of the residual friction coefficient were selected, namely $\mu_r = \mu_0$ (perfectly plastic response), $\mu_r = 0.8\mu_0$ (i.e., 20% degradation) and $\mu_r = 0.3\mu_0$.

The boundary conditions involved no friction at the end platens, while the localization was triggered by introducing an inhomogeneity in the center of the specimen (20% increase in the value of E). For the localized deformation mode, it was assumed that the shear band within an element forms at 57° with respect to the horizontal, which was the actual value measured in the experiment. Note that this value is lower than the usual estimate based on the Mohr–Coulomb criterion, that is, $45^\circ + \phi/2$, which is likely because the material displayed some inherent anisotropy. It is noted again that the orientation of the localization plane can, in general, be determined through an independent criterion, such as that associated with the bifurcation properties of the constitutive relation (cf. [43, 48]).

The main results of simulations are presented in Figures 11 and 12. Figure 11 shows the deformation mode, both the predicted and the experimentally observed, together with the corresponding material characteristics. The results of simulations are, in general, fairly consistent with the experimental data.

It is noted that the analysis presented previously employs a mesh that is oriented along the shear band in order to avoid potential numerical issues. In general, however, the results of simulations based on FEM/CLED are virtually independent of discretization, as the mathematical framework incorporates a characteristic dimension. In order to demonstrate this, a sensitivity analysis has been conducted employing, in addition to a previous mesh, two structured grids of different sizes. The results, which are shown in Figure 13, clearly indicate that the predicted localization patterns as well as the global mechanical characteristics are almost the same for all three types of FE meshes.

5.2.2. Modeling of shear band initiation and propagation in a cohesive slope subjected to foundation loading. The last example given here involves an assessment of stability of a slope in cohesive soil (overconsolidated silty clay) subjected to a foundation loading. The geometry adopted is shown Figure 14. The soil was modeled using a plasticity-based deviatoric hardening model [49, 50], while the foundation was assumed to be rigid-elastic. The material properties for the soil were taken as

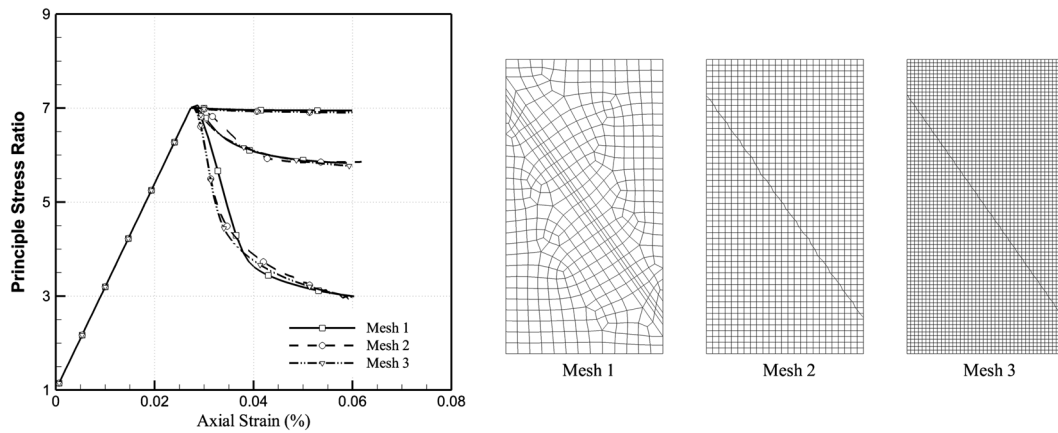


Figure 13. Mesh sensitivity analysis of shear band formation in biaxial compression test.

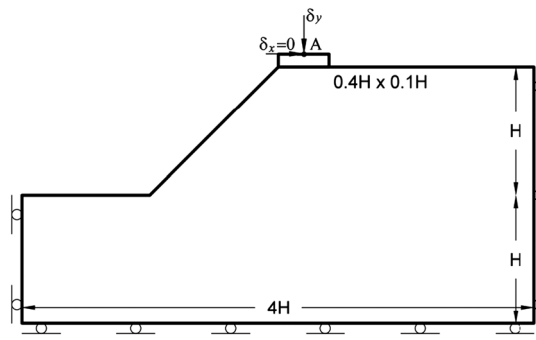


Figure 14. Geometry of the slope and the boundary conditions; $H = 10$ m.

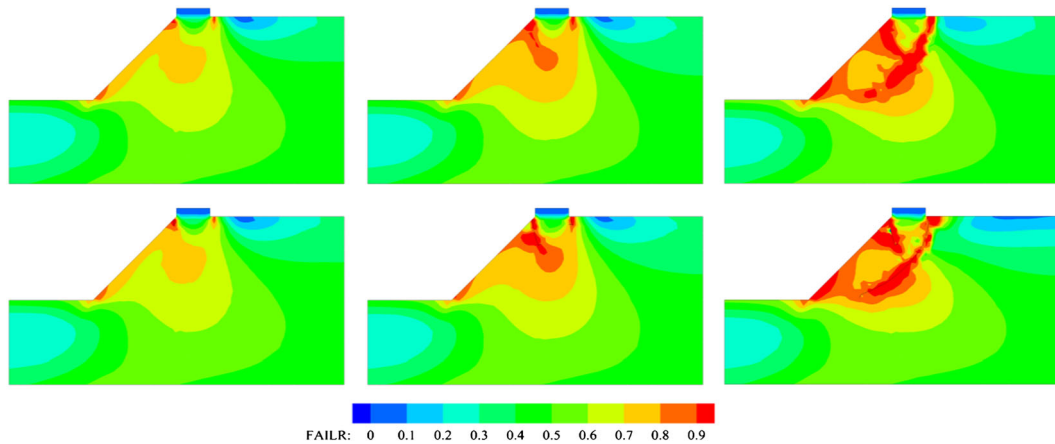


Figure 15. Failure ratio at different stages of shear band propagation; top: FEM/CLED; bottom: XFEM simulations.

$$E = 100 \text{ MPa}; \quad \nu = 0.35; \quad \eta_f = 0.98; \quad \eta_c = 0.77; \quad C = 40 \text{ kPa}; \quad A = 1.0 \times 10^{-5}$$

where η_f and η_c are the slope of the Mohr–Coulomb failure line and the dilation lines in p – q space, respectively, C is the cohesion, and A is the hardening parameter. For the interfacial properties, a cohesionless Mohr–Coulomb criterion was assumed, as described earlier. Here, the friction

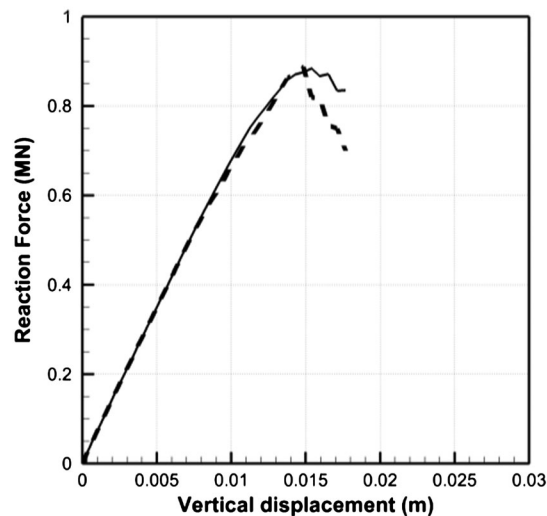


Figure 16. Force displacement response from both FEM/CLED and XFEM.

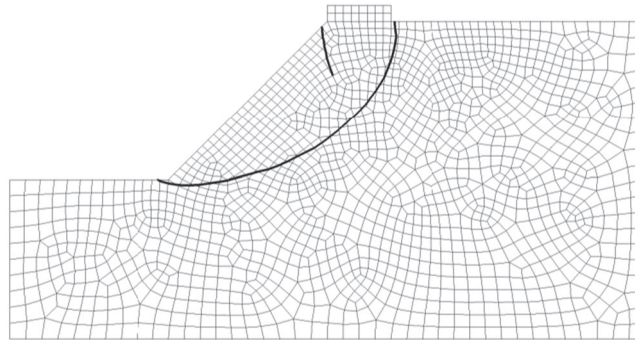


Figure 17. Shear band pattern.

coefficient is measured as $\tilde{\eta}_f = \tau/\sigma$, where σ and τ are normal and tangential values of traction acting along the interface at the onset of localization. A degradation of 30% over a sliding of 0.1 mm, along with $k_n = k_m = 10^{-8}$ N/m, was assumed for the interfacial model.

The boundary conditions are shown in Figure 14. The first step involved the analysis due to own weight of soil. Later, the foundation load was imposed through 100 increments. The criterion for the onset of localization was set as $\eta \rightarrow 0.9\eta_f$. The direction of the shear band was established as (i.e., $45 + \phi/2$) which corresponds to the orientation that maximizes the Coulomb failure function.

Figure 15 shows the distribution of the failure ratio η/η_f at three different stages of the loading process. The shear band is initiated at the left corner of the foundation. Subsequently, the main localized zone forms at the right-hand side and propagates until a complete failure of the slope. The load–displacement response and the cracking pattern at the end of simulation are plotted in Figures 16 and 17. Once again, it is evident that the value of the critical load triggering the loss of stability is virtually the same for both methodologies, that is, FEM/CLED and XFEM.

6. CONCLUDING REMARKS

The present study was focused on simulation of cohesive crack propagation as well as modeling of the onset and propagation of localized deformation associated with a shear band formation. The primary methodology employed here involved a constitutive relation with embedded discontinuity. A new formulation was presented based on the description of discontinuous motion, and an implicit

integration scheme was derived incorporating nonlinear properties of the intact material. The approach was coupled with the level-set method for explicit modeling of the discrete crack propagation process. Four different sets of numerical simulations were conducted. The first example involved cohesive mode I crack propagation. Next, a mixed-mode cracking was examined by simulating the experimental study of Galvez *et al.* [34]. Subsequently, the localized deformation associated with formation of a shear band was investigated. The analysis involved the simulation of a plane strain test on a granular material as well as the problem involving the assessment of slope stability. For all studied problems, a close correlation between the results from FEM/CLED and XFEM was achieved in terms of both the failure mechanism (that is, the cracking/shear band pattern) as well as the global load–displacement response; in particular, the assessment of ultimate load.

REFERENCES

1. Pietruszczak S, Mroz Z. Finite element analysis of deformation of strain-softening materials. *International Journal for Numerical Methods in Engineering* 1981; **17**(3):327–34.
2. Pietruszczak S. On homogeneous and localized deformation in water-infiltrated soils. *International Journal of Damage Mechanics* 1999; **8**(3):233–53.
3. Ngo D, Scordelis AC. Finite element analysis of reinforced concrete beams. *ACI Journal Proceedings* 1967; **64**(3):152–63.
4. Nilson AH. Nonlinear analysis of reinforced concrete by the finite element method. *ACI Journal Proceedings* 1968; **65**(9):757–66.
5. Ingraffea AR. Nodal grafting for crack propagation studies. *International Journal for Numerical Methods in Engineering* 1977; **11**(7):1185–7.
6. Saouma VE, Ingraffea AR, Gergely P, White RN. Interactive finite element analysis of reinforced concrete: a fracture mechanics approach. Cornell University, 1981.
7. Shephard MS, Yehia NA, Burd GS, Weidner TJ. Computational strategies for nonlinear and fracture mechanics problem. *Computers and Structures* 1985; **20**(1–3):211–23.
8. Rashid YR. Ultimate strength analysis of prestressed concrete pressure vessels. *Nuclear Engineering and Design* 1968; **7**(4):334–44.
9. Nayak GC, Zienkiewicz OC. Elasto-plastic stress analysis. A generalization for various constitutive relations including strain softening. *International Journal for Numerical Methods in Engineering* 1972; **5**(1):113–35.
10. Bažant ZP, Cedolin L. Blunt crack band propagation in finite element analysis. *Journal of the Engineering Mechanics* 1979; **105**(EM2):297–315.
11. Cedolin L, Bažant ZP. Effect of finite element choice in blunt crack band analysis. *Computer Methods in Applied Mechanics and Engineering* 1980; **24**:305–16.
12. Bazant ZP, Cedolin L. Finite element modeling of crack band propagation. *Journal of Structural Engineering* 1983; **109**:69–92.
13. Blandford GE, Ingraffea AR. Two-dimensional stress intensity factor computations using the boundary element method. *International Journal for Numerical Methods in Engineering* 1981; **17**:387–404.
14. Oliver J. Modelling strain discontinuities in solid mechanics via strain softening constitutive equations. Part 1: fundamentals. *International Journal for Numerical Methods in Engineering* 1996; **39**(21):3575–600.
15. Belytschko T, Fish J, Engelmann BE. A finite element with embedded localization zones. *Computer Methods in Applied Mechanics and Engineering* 1988; **70**(1):59–89.
16. Simo JC, Oliver J, Armero F. An analysis of strong discontinuities induced by strain-softening in rate-independent inelastic solids. *Computational Mechanics* 1993; **12**(5):277–96.
17. Belytschko T, Lu YY, Gu L. Element-free Galerkin methods. *International Journal for Numerical Methods in Engineering* 1994; **37**(2):229–56.
18. Liu WK, Jun S, Zhang YF. Reproducing kernel particle methods. *International Journal for Numerical Methods in Engineering* 1995; **20**(8–9):1081–106.
19. Liu WK, Li S, Belytschko T. Moving least-square reproducing kernel methods (I) methodology and convergence. *Computer Methods in Applied Mechanics and Engineering* 1997; **143**:113–54.
20. Melenk JM, Babuška I. The partition of unity finite element method: basic theory and applications. *Computer Methods in Applied Mechanics and Engineering* 1996; **139**(1):289–314.
21. Belytschko T, Black T. Elastic crack growth in finite elements with minimal remeshing. *International Journal for Numerical Methods in Engineering* 1999; **45**:601–20.
22. Moës N, Dolbow J, Belytschko T. A finite element method for crack growth without remeshing. *International Journal for Numerical Methods in Engineering* 1999; **46**(1):131–50.
23. Sukumar N, Moës N, Moran B, Belytschko T. Extended finite element method for three-dimensional crack modelling. *International Journal for Numerical Methods in Engineering* 2000; **48**(11):1549–70.
24. Sukumar N, Chopp DL, Moës N, Belytschko T. Modeling holes and inclusions by level sets in the extended finite-element method. *Computer Methods in Applied Mechanics and Engineering* 2001; **190**(46):6183–200.

25. Stolarska M, Chopp DL, Moës N, Belytschko T. Modelling crack growth by level sets in the extended finite element method. *International Journal for Numerical Methods in Engineering* 2001; **51**(8):943–60.
26. Belytschko T, Chen H, Xu J, Zi G. Dynamic crack propagation based on loss of hyperbolicity and a new discontinuous enrichment. *International Journal for Numerical Methods in Engineering* 2003; **58**(12):1873–905.
27. Réthoré J, de Borst R, Abellan M-A. A two-scale approach for fluid flow in fractured porous media. *International Journal for Numerical Methods in Engineering* 2006; **71**(7):780–800.
28. Khoei AR, Haghighat E. Extended finite element modeling of deformable porous media with arbitrary interfaces. *Applied Mathematical Modelling* 2011; **35**:5426–41.
29. Mohammadnejad T, Khoei AR. Hydro-mechanical modeling of cohesive crack propagation in multiphase porous media using the extended finite element method. *International Journal for Numerical and Analytical Methods in Geomechanics* 2012; **37**(10):1247–79.
30. Areias PMA, Belytschko T. Two-scale method for shear bands: thermal effects and variable bandwidth. *International Journal for Numerical Methods in Engineering* 2007; **72**(6):658–96.
31. Zamani A, Eslami MR. Implementation of the extended finite element method for dynamic thermoelastic fracture initiation. *International Journal of Solids and Structures* 2010; **47**(10):1392–404.
32. Khoei AR, Moallemi S, Haghighat E. Thermo-hydro-mechanical modeling of impermeable discontinuity in saturated porous media with X-FEM technique. *Engineering Fracture Mechanics* 2012; **96**(96):701–23.
33. Dolbow J, Moës N, Belytschko T. An extended finite element method for modeling crack growth with frictional contact. *Computer Methods in Applied Mechanics and Engineering* 2001; **190**(51):6825–46.
34. Liu F, Borja RI. A contact algorithm for frictional crack propagation with the extended finite element method. *International Journal for Numerical Methods in Engineering* 2008; **76**(10):1489–512.
35. Borja RI. A finite element model for strain localization analysis of strongly discontinuous fields based on standard Galerkin approximation. *Computer Methods in Applied Mechanics and Engineering* 2000; **190**(11–12):1529–49.
36. Sanborn SE, Prévost JH. Frictional slip plane growth by localization detection and the extended finite element method (XFEM). *International Journal for Numerical and Analytical Methods in Geomechanics* 2010; **35**(11):1278–98.
37. Benson DJ, Bazilevs Y, De Luycker E. A generalized finite element formulation for arbitrary basis functions: from isogeometric analysis to XFEM. *International Journal for Numerical Methods in Engineering* 2010; **83**(6):765–85.
38. Oliver J, Huespe AE, Blanco S, Linero DL. Stability and robustness issues in numerical modeling of material failure with the strong discontinuity approach. *Computer Methods in Applied Mechanics and Engineering* 2006; **195**(52):7093–114.
39. Gálvez JC, Elices M, Guinea GV, Planas J. Mixed mode fracture of concrete under proportional and nonproportional loading. *International Journal of Fracture* 1998; **94**(3):267–84.
40. Alshibli KA, Sture S. Shear band formation in plane strain experiments of sand. *Journal of Geotechnical and Geoenvironmental Engineering* 2000; **126**(6):495–503.
41. Zi G, Song J-H, Budyn E, Lee S-H, Belytschko T. A method for growing multiple cracks without remeshing and its application to fatigue crack growth. *Modelling and Simulation in Materials Science and Engineering* 2004; **12**(5):901–15.
42. Simo J. Computational Inelasticity. Springer Verlag: New York, 1998.
43. Rudnicki JW, Rice JR. Conditions for the localization of deformation in pressure-sensitive dilatant materials. *J Mech Phys Solids* 1975; **23**(6):371–94.
44. Pietruszczak S, Mroz Z. On failure criteria for anisotropic cohesive-frictional materials. *International Journal for Numerical and Analytical Methods in Geomechanics* 2001; **25**(5):509–24.
45. Leguillon D. Strength or toughness? A criterion for crack onset at a notch. *European Journal of Mechanics—A/Solids* 2002; **21**(1):61–72.
46. Chessa J, Belytschko T. An enriched finite element method and level sets for axisymmetric two-phase flow with surface tension. *International Journal for Numerical Methods in Engineering* 2003; **58**(13):2041–64.
47. Wells GN, Sluys LJ. Three-dimensional embedded discontinuity model for brittle fracture. *International Journal of Solids and Structures* 2000; **38**(5):897–913.
48. Song X, Rechenmacher AL, Abedi S. Shear band in sand with spatially varying density. *Journal of the Mechanics and Physics of Solids* 2013; **61**:219–34.
49. Pietruszczak S. Fundamentals of Plasticity in Geomechanics. CRC Press: Balkema, 2010.
50. Pietruszczak S, Haghighat E. Assessment of slope stability in cohesive soils due to a rainfall. *International Journal for Numerical and Analytical Methods in Geomechanics* 2013; **37**:3278–92.